Journal of Materials Chemistry A

Synthesis and Characterization of Co2-xRhxP Nanoparticles and Their Catalytic Activity Towards the Oxygen Evolution Reaction.

Journal:	*Journal of Materials Chemistry A*
Manuscript ID	TA-ART-03-2018-002016.R2
Article Type:	Paper
Date Submitted by the Author:	04-Jun-2018
Complete List of Authors:	Mutinda, Samuel; Wayne State University, Department of Chemistry Li, Da; Wayne State University, Department of Chemistry Kay, Jacob; Wayne State University, Department of Chemistry Brock, Stephanie; Wayne State University, Department of Chemistry

SYNTHESIS AND CHARACTERIZATION OF $Co_{2-x}Rh_xP$ NANOPARTICLES AND THEIR CATALYTIC ACTIVITY TOWARDS THE OXYGEN EVOLUTION REACTION

Samuel I. Mutinda, Da Li, Jacob Kay and Stephanie L. Brock*
Wayne State University, Detroit, MI 48202
**E-mail: sbrock@chem.wayne.edu*

Abstract

We show that $Co_{2-x}Rh_xP$ ternary phase nanoparticles can be synthesized using the arrested precipitation technique, via a requisite low temperature co-reduction of Co^{2+} and Rh^{3+} ions, followed by phosphidation of the resulting intermediate product at above 300°C. The most unique aspect of our synthesis protocol is the fact that we are able to solubilize both cubic antifluorite and orthorhombic crystal systems, into uniform solid solutions of $Co_{2-x}Rh_xP$ nanoparticles under mild reaction conditions. These nanoparticles are active towards the oxygen evolution reaction and deliver higher electrolytic activities as compared to those of Co_2P and Rh_2P binary phases. Cobalt-rich compositions were found to be the most active, with a sweet spot occurring at a target composition of $Co_{1.75}Rh_{0.25}P$, where a current density of 10 mA/cm^2 was achieved at an overpotential of 0.29 V.

Keywords: phosphide, water splitting, oxygen evolution, nanoparticles, electrocatalysis

Introduction

Transition metal phosphides (TMP's) present a rich diversity of physical and chemical properties that can be tailored for different applications, and are gaining relevance in hydroprocessing (hydrodesulfurization, hydrodenitrogenation, etc.), metallurgy and electrocatalysis, among other fields.[1-6] Fundamental studies have shown that their structure, composition and stoichiometry dictate their properties, with both monophosphides (i.e. MP) and the metal-rich species (i.e. $M_{>1}P$) being metallic in nature, while the phosphorus-rich compositions (i.e. $MP_{>1}$) are of covalent character.[7-9] Their composition-dependent functionality underscores the importance of developing simple and reliable synthetic protocols that can be used to accurately and effectively target different compositions and stoichiometries.

Researchers have successfully developed several synthetic protocols for targeting a wide range of TMP's at the nanoscale, due to the many benefits that are known to accrue from such a small size regime, including the enhanced catalytic activity associated with high surface area formulations. While approaches to binary phase nanoparticles of a number of metals and compositions have been reported over the years, ternary (bimetallic) phosphide nanoparticles have only recently appeared.[10-13] In general, these ternary phases are found to outperform the binary end phases reflecting the greater versatility in engineering the electronic characteristics of catalytic sites and formation of multimetallic active sites.[10-13] A key challenge to the synthesis of such ternary phases lies in the reactivity differences of the two metals being combined, which can lead to phase segregation and/or limit the ability to rationally dial in the desired composition.

TMP nanomaterials for catalysis have traditionally been synthesized using the temperature programmed reduction (TPR) technique,[10] which among other limitations, does not easily allow for particle morphology and size control. Our group has been at the forefront of addressing these challenges and has in the past shown that both monometallic and bimetallic phosphides, such as Ni_2P, $Ni_{2-x}Co_xP$ and $Ni_{2-x}Fe_xP$, can be synthesized using the solution-phase arrested precipitation technique. We have shown that this technique can be used to synthesize highly monodisperse phosphide nanoparticles, where particle morphology and size can be tuned by adjusting different reaction levers e.g. reaction temperature or reactants concentration.[11-13]

Intriguingly, the available publications on ternary phosphides have been largely limited to non-noble metals,[8, 10-13] even though noble metal-based binary phosphides are known to exhibit high activity for catalytic reactions such as hydroprocessing.[14, 15] As demonstrated in metal alloy phases, noble-metal reactivity can be achieved in base-metal formulations at low concentrations of the more expensive, and less earth-abundant, noble metal component.[16, 17] However, in terms of establishing a rational synthetic approach, the combination of base-metal and noble-metal in a ternary phosphide is particularly challenging because the chemical reactivity of the two components is so dissimilar. Recently, we have shown that ternary phosphides of $Ni_{2-x}Ru_xP$ can be prepared as discrete nanoparticle formulations, with crystallinity achieved at the Ni-rich end of the spectrum (Ru_2P nanoparticles prepared by arrested precipitation are themselves amorphous). These phases proved to be quite active for water oxidation, with x = 0.75 exhibiting a lower overpotential at a current density of 10 mA/cm^2 (0.34V) than Ni_2P nanoparticles prepared similarly (0.44 V).[18]

The present work reports on the synthesis and characterization of ternary phase $Co_{2-x}Rh_xP$ nanoparticles for electrolytic water oxidation, using the solution-phase arrested precipitation technique. The relatively low cost and earth abundance of cobalt, coupled with the ability of rhodium to promote the activity of Co_2P, are some of the major motivators for this work. In contrast to $Ni_{2-x}Ru_xP$, the bulk phase diagram of $Co_{2-x}Rh_xP$ is largely unknown, with only one composition reported, namely Co_1Rh_1P.[19, 20] Thus, the most significant contribution of this work is perhaps the fact that we were able to form a wide range of $Co_{2-x}Rh_xP$ solid solutions at the nanoscale for the first time, by solubilizing crystal systems that clearly differ extensively. Co_2P and Rh_2P systems crystallize in the orthorhombic (Fe_2P-type) and cubic (antifluorite-type) structures respectively, and exhibit major structural disparities that may favor phase separation. In addition to developing a synthetic protocol for the above mentioned nanoparticles, our work also presents preliminary results on their electrolytic activity towards the Oxygen Evolution Reaction (OER, water oxidation). We show that incorporation of small amounts of Rh (x = 0.25) has a profound effect on the activity of Co_2P towards water oxidation.

Experimental

1. Materials:

All chemicals were utilized as received. $Co(acac)_2$ (99%) and $RhCl_3 \cdot nH_2O$ (38-40% Rh) were purchased from Acros Organics and Sigma Aldrich, respectively, while 1-octadecene (90%) and oleylamine (>50%) were obtained from Sigma Aldrich and TCI America, respectively. Tri-octylphosphine (TOP, 97%) was obtained from STREM chemicals and ethanol (200 proof) was

purchased from Decon Laboratories. Chloroform was obtained from Fischer Scientific and Nafion (5 wt%, LQ-1105) was acquired from Ion Power.

2. Synthesis:

$Co_{2-x}Rh_xP$, Rh_2P and Co_2P nanoparticles were prepared via the arrested precipitation technique, where either $Co(acac)_2$ or $Co_2(CO)_8$ and $RhCl_3{\cdot}H_2O$ were used as the Co and Rh metal precursors respectively, while tri-octylphosphine (TOP) was used as the phosphorus source. 1-octadecene was used as the high boiling point solvent while oleylamine was employed as both a co-solvent and a reducing agent.

(a) $Co_{2-x}Rh_xP$

A wide range of compositions of $Co_{2-x}Rh_xP$ nanoparticles were synthesized by quantitatively adjusting the amounts of $Co(acac)_2$ and $RhCl_3{\cdot}nH_2O$ metal precursors, while targeting 0.19 mmol of the final product in each reaction. For example, in the synthesis of $Co_{1.75}Rh_{0.25}P$ nanoparticles, 0.0875g (0.34 mmols) of $Co(acac)_2$ and 0.01g (0.048 mmols) of $RhCl_3{\cdot}nH_2O$ were utilized, in targeting 0.19 mmols of the ternary phase nanoparticles. In a typical setting, the two metal precursors were dissolved in a solvent mixture of 5 mL 1-octadecene and 15 mL oleylamine, after which the solution was degassed at 110 ^oC for 30 minutes, and purged several times with argon. The reaction mixture was then brought to 230^oC and aged for 9 hours, after which 6 mL of TOP was injected into the mixture and the reactants aged for an additional 3 hours at the same temperature. The reaction temperature was then increased to between 310^oC to 350^oC for a typical duration of 3 hours, after which the product was allowed to cool down to room temperature. The black product was then washed using a mixture of chloroform and ethanol and recovered using centrifugation. *Specific temperature and time parameters used to produce X-ray phase-pure materials, as a function of x, are shown in Table S1 (ESI)†.*

(b) Rh_2P

0.08 g (0.38 mmols) of $RhCl_3{\cdot}nH_2O$ was dissolved into a solvent mixture of 5 mL 1-octadecene and 15 mL oleylamine, then degassed at 110^oC for 30 minutes, followed by aging at 230^oC for 1.5 hours. 6 mL of TOP was then injected into the black solution, after which the temperature was increased to 350^oC. The reaction mixture was then held at this temperature for 3 hours after which the product was cooled down, washed and recovered as described above.

(c) Co_2P

0.16 g (0.44 mmols) of $Co_2(CO)_8$ was dissolved into a degassed solvent mixture of 15 mL 1-octadecene and 3 mL oleylamine, after which the mixture was aged at 200^oC for 1.5 hours. 0.2 mL of TOP was then injected into the black solution, after which the temperature was increased to 300^oC and held constant for 1.5 hours. The product was then allowed to cool down, washed and recovered in the same way as outlined above.

3. Ink preparation for water oxidation electrocatalysis:

Catalyst ink was prepared by suspending carbon-black-supported nanoparticles in a mixture of water, ethanol, isopropanol and 5% Nafion solution. In a typical preparation, 10 mg of ligand stripped $Co_{2-x}Rh_xP$ nanoparticles were mixed with 5 mg of carbon-black powder and sonicated in hexane (10 mL) for 30 minutes. 20 mL of ethanol was then added to the suspension and the

carbon-nanoparticle mixture recovered by centrifugation. The sonication and centrifugation steps were repeated another two times, after which the recovered mixture was dried under vacuum. The sample was then transferred to a ceramic boat, where it was heated in a tube furnace under 5% H_2/Ar gas flow at 400^{o}C for 1 hour. At this point, the sample was cooled down to room temperature and the ink prepared as follows: The annealed mixture was suspended in 2 mL of ethanol and sonicated for 20 minutes, after which 1 ml of nano-pure H_2O and 1 mL of isopropanol were added and the mixture sonicated for another 20 minutes. 1 mL of Nafion solution was then added and the mixture sonicated for another 20 minutes in order to achieve maximum ink uniformity.

4. Characterization:

Techniques that were employed in this study comprise: X-ray powder diffraction (XRD), transmission electron microscopy (TEM), energy dispersive x-ray spectroscopy (EDX), x-ray photoelectron spectroscopy (XPS), inductively coupled plasma mass spectroscopy (ICP-MS) and three-electrode cyclic voltammetry.

XRD was performed using a Bruker Phaser II instrument, in which a scanning range of 35^o to 60^o (2θ), a sampling width of 0.010^o and a scanning duration of 1.25 seconds per step were utilized. The Jade software was used to calculate the samples' Scherrer crystallite sizes while the fitted (hkl) peak positions were used to quantify lattice constant changes.

TEM data were collected using a JEOL 2010 instrument that was equipped with an EDX and annular dark-field detectors, and was operated at an accelerating voltage of 200 kV. In a typical sample preparation procedure, a small portion of the solid sample of interest was dispersed in chloroform and sonicated for at least 30 minutes, after which a few drops were pipetted onto a copper grid and the grid allowed to air dry.

XPS measurements were performed on a Kratos Axis Ultra XPS system where a representative as-prepared carbon-supported catalyst ($Co_{1.75}Rh_{0.25}P$) was analyzed in its native powdered form while the post-catalysis sample was analyzed on a carbon cloth substrate.

ICP-MS analyses were also performed on the representative samples described above, before and after catalysis, using an Agilent 7700 instrument. The sample was dissolved in concentrated nitric acid and diluted using nano-pure water. A calibration curve was established using standards for Co, Rh and P.

Electrochemical measurements were carried out in 1M KOH on an EC epsilon potentiostat that was equipped with a glassy carbon rotating disc electrode, a Ag/AgCl reference electrode and a platinum wire counter electrode. In a typical measurement, 10uL of catalyst ink was drop cast on a clean glassy carbon electrode that had a surface area of 0.07 cm^2, and dried under a IR lamp. Cyclic voltammetry measurements were then performed at a scan rate of 10 mV/s and at 1600 rotations per minute after which the data were converted from the Ag/AgCl to the reversible hydrogen electrode (RHE) scale for comparison. Long term stability tests were performed at a constant potential of 0.55 V for a duration of 50 hours in a two compartment H-type cell that was equipped with a frit, and at a pH of 14. A coiled Pt wire was used as the counter electrode while a Ag/AgCl electrode was used as the reference. For this particular measurement, the catalyst ink was deposited on a geometrical area of 1 cm^2 carbon cloth substrate. Before ink deposition, the carbon cloth was treated at 450 ^{o}C for 2 hours in air in order to burn off any residual organic

materials and improve surface wettability. Faradaic efficiency was performed in a similar manner at 0.65 V on a geometric substrate area of 4cm^2 for 65 minutes after which the head space gas composition was quantified using a GOW-MAC series 400 gas chromatograph that was equipped with a TCD detector. A blank analysis in which only carbon ink was deposited on the substrate was also performed in a similar manner, in order to accurately calculate the efficiency. Helium gas was used as the carrier gas at a flow rate of 30 mL per minute while nitrogen gas was used as the internal standard.

Results and Discussion

Synthetic protocol evaluation:

A significant portion of our study focuses on the preparation of $Co_{2-x}Rh_xP$ ternary phase nanoparticles, although the Co_2P and Rh_2P binary phase counterparts were also prepared for comparison and elucidation purposes. All synthesis were performed under standard Schlenk line conditions, and in a solvent mixture of 1-octadecene and oleylamine, where the former served as a high boiling and non-coordinating solvent and the latter was used both as a stabilizer and a reducing agent.[11, 13] $Co_{2-x}Rh_xP$ nanoparticles were synthesized in a two-step process beginning with co-reduction of $Co(acac)_2$ and $RhCl_3{\cdot}nH_2O$ precursors to form Co-Rh nanoparticles, followed by a hot injection of trioctylphosphine (TOP) to yield the desired $Co_{2-x}Rh_xP$ nanoparticles. The general strategy for this protocol is similar to one that was previously reported by our group for other transition metal ternary phosphides, where the formation of metal alloys or mixtures preceded the evolution of the phosphide nanoparticles.[11, 13] In the optimized reaction conditions, the co-reduction of the metal precursors was performed in the above mentioned solvent mixture at 230^{o}C for a duration of 9 hours, while phosphidation was performed at between 310-350^{o}C for 3 hours. In addition, the composition of the nanoparticles was adjusted by quantitatively varying the amounts of the metal precursors, while maintaining the amount of TOP constant. Co_2P nanoparticles were synthesized in a similar manner to that reported by Robinson's group, where $Co_2(CO)_8$ and (TOP) were used as the cobalt and phosphorus sources, respectively.[21] Rh_2P nanoparticles, on the other hand, were synthesized by employing $RhCl_3{\cdot}nH_2O$ as the metal precursor. The first step entailed reducing Rh^{3+} ions to Rh^0 at 230^{o}C for 1.5 hours, followed by the injection of TOP and ramping to 350^{o}C, where the temperature was held constant for 3 hours. This synthesis strategy is similar to the one that was reported by the Schaak group, except that theirs was a two-pot process.[22]

Crystal structure and morphology:

Fig. 1 compares the Powder X-ray Diffraction (PXRD) data for pure Co_2P and Rh_2P nanoparticles with those of the different $Co_{2-x}Rh_xP$ nanoparticles that were prepared, with the x values depicting the targeted compositions in the different samples. Co_2P and cobalt rich compositions (up to $x \leq 0.75$) adopt the orthorhombic Co_2P structure (PDF # 00-032-0306), and are mainly defined by the peak that occurs at ~41° (2Θ), as a result of an overlap between the (121) and (201) peaks. Rh_2P and the rhodium rich compositions ($x > 1$), on the other hand, adopt the cubic antifluorite structure (PDF # 01-071-6466), and are largely defined by the (220) peak that occurs at ~46° (2Θ). Occurring between these two regimes is the Co_1Rh_1P composition that largely conforms to the antifluorite structure.

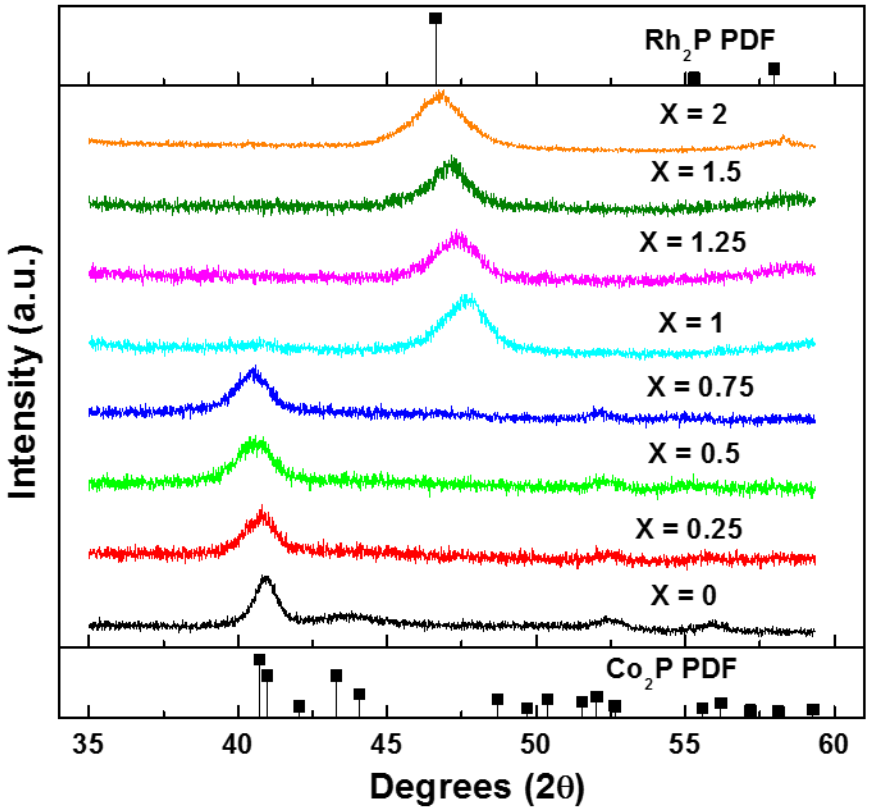

Fig. 1: PXRD data for Co_2P, Rh_2P and $Co_{2-x}Rh_xP$ nanoparticles showing the targeted values of x. Reference patterns for Co_2P and Rh_2P are also shown.

Table S2 (ESI)† provides a summary of Energy Dispersive X-ray (EDX) spectroscopy data that were collected from the ternary phase nanoparticles. As evidenced here, the calculated compositions are close to the targeted ones, with differences between the targeted and actual Rh content ranging from 4-12%.

The shifts in the overlapped peaks that occur at ~40° (2Θ) in the cobalt-rich compositions, or the (220) peak shifts in the rhodium-rich compositions, are consistent with the expected changes in lattice parameters: Progressive incorporation of Rh ions leads to an incremental lattice expansion, and hence the progressive reduction in the observed diffraction angles. Despite the fact that Co_1Rh_1P is reported to adopt the Co_2P structure in the bulk phase, our targeted x = 1 nanoparticles (which are actually slightly Co-rich; 1.1:0.9 Co:Rh) primarily adopt the antifluorite structure, although the slight rise ~40° (2Θ) (indicative of a Co_2P-type phase) reflect minor phase segregation suggesting we are close to the structural transition.[19, 20] Peaks for samples where $x \geq 1$ were fit to determine the Scherrer sizes and the d-spacing changes (increasing) that occur in the antifluorite structure type with increasing Rh, as shown in Table S3 (ESI)†. These data are consistent with the EDS data and support the conclusion that the samples are indeed solid solutions. Data corresponding to Co_2P-type materials were not fit due to issues with deconvoluting the broad, overlapping peaks.

There are fundamental structural differences between the Rh_2P and Co_2P structures that are worth pointing out. As shown in Fig 2(a), the Co_2P orthorhombic structure is defined by two metal sites, in which the first one (M_1 – shown in purple) is surrounded by four phosphorus

atoms (shown in blue) in a tetrahedral symmetry, while the second one (M_2 – shown in gold) is surrounded by five phosphorus atoms, in a square pyramidal symmetry. Phosphorus on the other hand is surrounded by nine metal atoms in a tri-capped trigonal prismatic symmetry. In principle, the smaller metal ion is expected to reside in the tetrahedral site while the larger cation occupies the square pyramidal site. The significant covalent radius difference between Rhodium (1.35 Å) and Cobalt atoms (1.26 Å) is expected to be a strong driving force towards this type of ordering.[3, 11, 23] On the other hand, Rh ions in the Rh_2P structure are all defined by a single metal site (shown in pale yellow), and reside in tetrahedral holes, while P ions (shown in green) occupy cubic positions.[14] Our data suggest that, despite the significant differences in structure, there is a large solid-solution region in the Co_2P-Rh_2P phase diagram, and minimal phase segregation is evident.

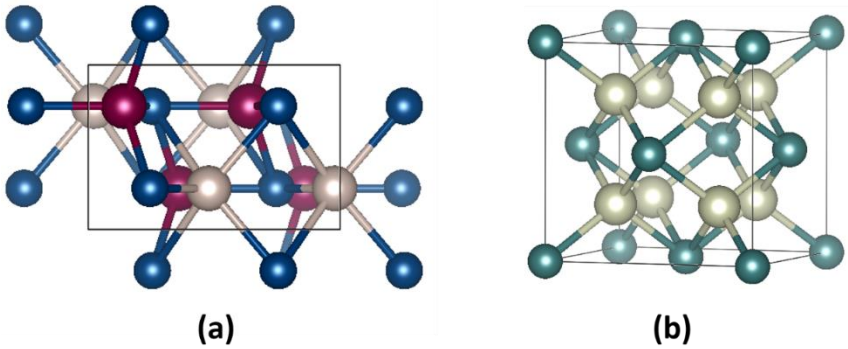

Fig. 2: Ball and stick models for the crystal structures of (a) Co_2P and (b) Rh_2P

Fig. 3 provides a summary of the Transmission Electron Microscopy (TEM) data corresponding to Co_2P, $Co_{2-x}Rh_xP$ and Rh_2P nanoparticles. According to the images, Co_2P nanoparticles are characterized by an average size of 15 nm while Rh_2P nanoparticles are much smaller, with an average size of 4 nm. All the cobalt-rich $Co_{2-x}Rh_xP$ nanoparticles (adopting the orthorhombic structure type) have an average particle size of 10 nm, while the rhodium-rich ones (cubic, antifluorite) are characterized by an average size of 5 nm. These size similarities occur irrespective of the different compositions within each phase, as supported by PXRD data, and may be a consequence of different nucleation and growth conditions in the different phases. Co_2P and the cobalt-rich $Co_{2-x}Rh_xP$ samples seem to be discrete and well-dispersed in nature, while the rhodium-rich and the Rh_2P nanoparticles are clustered together. This agglomeration is thought to be a spontaneous process that occurs as the ~ 4-5 nm high surface area nanoparticles seek to lower their surface energy. Such agglomeration has also been reported by other groups, and has been sited to arise from a balance between attractive and repulsive forces that may exist among different small precursor nanoparticles.[24, 25]

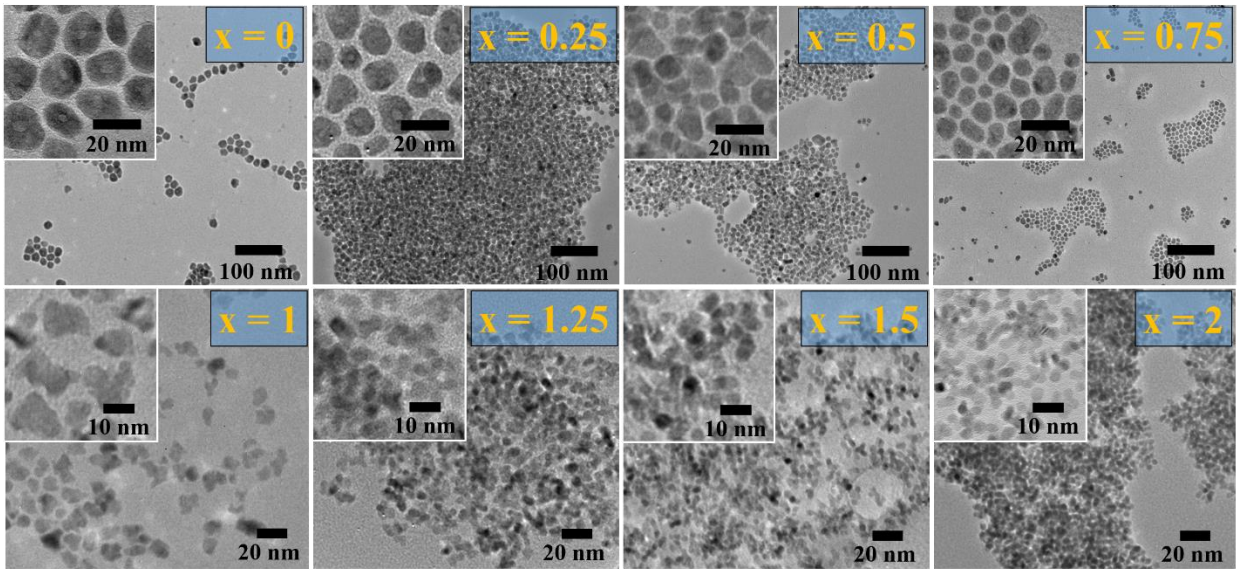

Fig. 3: TEM data for different $Co_{2-x}Rh_xP$ nanoparticles. Corresponding histograms are shown Fig. S1 (ESI)†

The morphology of Co_2P nanoparticles can be described as spherical in nature, with hollow voids, which can be attributed to the Kirkendall effect.[21, 22] Rh_2P nanoparticles, on the other hand, can be described as spherical in nature, and without any hollow features. The lack of hollow voids in these nanoparticles is attributed to their small size, as was reported by Schaak's group, where the formation of hollow features in transition metal phosphides was found to be disfavored by small crystallite size i.e. < 5 nm.[22] The morphology of $Co_{2-x}Rh_xP$ nanoparticles can generally be described as quasi spherical, with diminishing hollow features as more Rh is incorporated into the structure. Nanoparticles with a metal ratio of 1:1 reveal considerable polydispersity in their size and shape, most likely due to the subtle phase separation that occurs at this composition, as was discussed previously (Fig. 1). Shown in Fig. 4(a) – (c) are high resolution TEM images for representative target nanoparticle compositions, namely $Co_{1.75}Rh_{0.25}P$, $Co_{1.25}Rh_{0.75}P$ and Rh_2P. As evidenced by the data, all the images are characterized by clearly discernable and ordered lattice fringes, which is indicative of the samples' crystallinity. The size range of the fringes in the ternary phase compositions could either be attributed to the (121) and (201) crystal planes in the Co_2P structure,[26, 27] while those that are shown in Fig. 4(c) could be attributed to the (200) planes in the Rh_2P structure.[28, 29] The slight difference in lattice fringe size between Figs. 4(a) and (b) is attributed to the difference in the unit cell size, consistent with the PXRD peak shifts in Fig. 1.

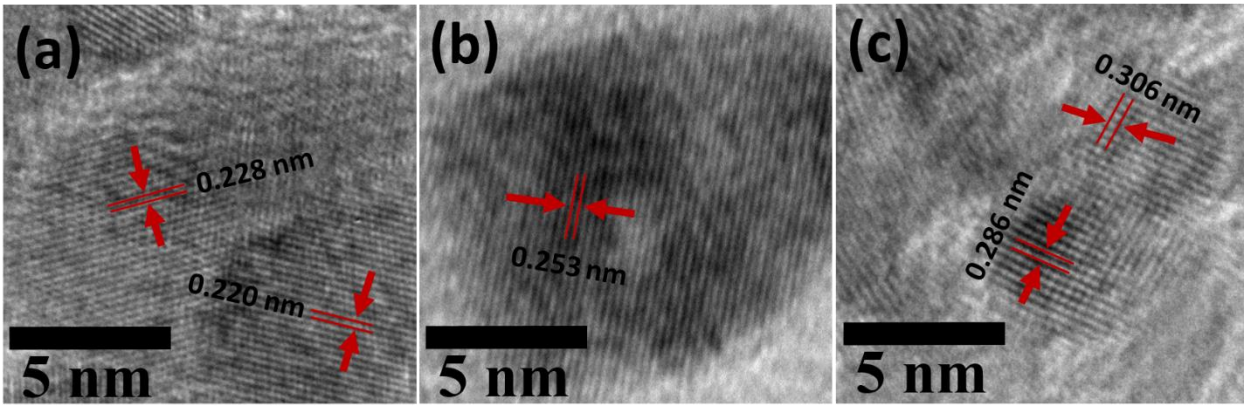

Figure 4: High resolution TEM data for (a) $Co_{1.75}Rh_{0.25}P$, (b) $Co_{1.25}Rh_{0.75}P$ and (c) Rh_2P nanoparticles

In order to ascertain the distribution of elements within the $Co_{2-x}Rh_xP$ nanoparticles, STEM/EDS mapping data were acquired on a representative sample in which the targeted composition was $Co_{1.75}Rh_{0.25}P$. As can be seen from Fig. 5, the Energy Dispersive Spectroscopy (EDS) line scan and elemental mapping data reveal that the three elements (Co, Rh and P) have a uniform distribution within the nanoparticles. The high angle annular dark field (HAADF) image is consistent with this interpretation, since the nanoparticles are characterized by a uniform and non-directional Z-contrast. Generalizing these observations to the rest of the samples, it can be argued that the samples are solid solutions, as suggested by the PXRD data (Fig. 1).

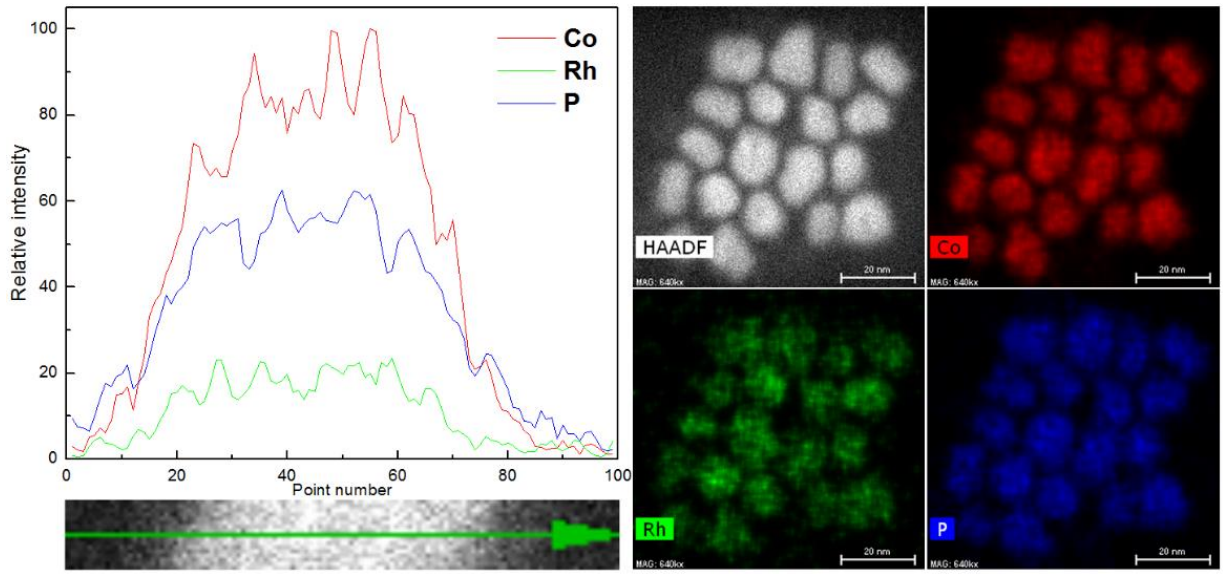

Fig. 5: EDS line scan, high angle annular dark field (HAADF) and elemental mapping data for $Co_{1.75}Rh_{0.25}P$. The scale bars (right) correspond to 20 nm.

Mechanistic Evaluations

Preliminary investigations revealed that the co-reduction of the two metal precursors in the presence of TOP hinders the formation of the desired ternary phase nanoparticles, with the resulting product being Co-rich, while co-reducing the precursors in the absence of TOP for a

certain period of time, followed by a hot injection of TOP, favors the incorporation of Rh into the Co_2P structure, hence leading to the formation of the desired $Co_{2-x}Rh_xP$ composition. As an example, we targeted a representative composition $Co_{1.25}Rh_{0.75}P$, with and without TOP at the reaction onset. As shown in Fig. 6, it was established through PXRD, TEM and EDS data that co-reducing the precursors in the presence vs. the absence of TOP, while maintaining all other reaction parameters constant, had clear consequences on both the morphology and composition of the final product. PXRD data taken from products conceived in the initial presence of TOP matched exactly the pattern and peak positions expected for Co_2P, whereas when TOP was initially absent, the peak pattern is the same, but the peaks are shifted to lower 2-theta, indicative of Rh incorporation (Fig. 6a). These data are corroborated by the TEM and EDS data (Fig. 6b). When TOP is present from the beginning, a star-like morphology results with minimal Rh inclusion (ca 10% of the targeted quantity). According to Robinson's group, star-like crystals can arise in Co_2P from a ligand-directed cyclic twinning mechanism, in which nanorods that undergo prior crystal splitting form the arms of the particles,[30] as is also seen in our data. In contrast, when TOP is added after Co and Rh are allowed to react at the intermediate 230 °C temperature, all of the Rh is incorporated (107% of the targeted quantity) and the particles adopt a quasi-spherical morphology. This clearly indicates that incorporating TOP at the onset of the reaction retards the incorporation of Rh into Co_2P, rendering Rh largely unreactive.

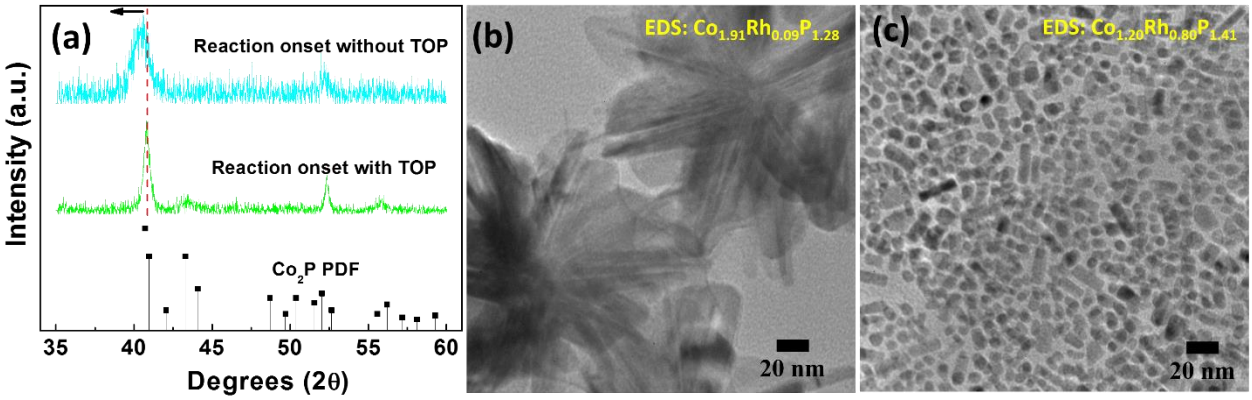

Fig. 6: (a) PXRD and TEM data of $Co_{1.25}Rh_{0.75}P$ target composition showing the effect of (b) presence and (c) absence of TOP during the co-reduction process

Since TOP has been reported to bind to transition metal precursors at the early stages of the arrested precipitation reaction, forming metal-phosphine complexes that eventually undergo thermal decomposition at later stages,[31, 32] we surmise that a difference in the reactivity of such a complex or complexes dominates when TOP is incorporated at the reaction onset, effectively rendering Rh unreactive. We hypothesize that the co-reduction of the two metal precursors in the absence of TOP may yield a reactive intermediate that is requisite to the formation of the desired ternary phase nanoparticles, upon phosphidation. As has been discussed extensively by Li's group, the co-reduction of a mixture of a noble and non-noble metal precursors proceeds in such a manner that the noble metal ions undergo reduction first, after which they start acting as "bridges" for the transfer of electrons from the electron donor, to the base metal ions. In our case for example, Rh atoms are expected to continuously deliver electrons from oleylamine to Co^{2+} ions in a way that effectively results in the progressive transfer of electron density from rhodium to cobalt, until all the Co^{2+} ions are reduced.[16, 17] It is possible that TOP binds tightly to Rh, interfering with its ability to react with/reduce Co. Indeed, prior work in our group on $Ni_{2-x}Ru_xP$

revealed that Ru was also "deactivated" when TOP was incorporated at the outset; to form the desired phase, Ru was reduced initially at 230 °C, then the Ni and TOP precursors were added together.[18] With respect to the Co-Rh-P phases investigated here, as shown in Fig. 7, the precursor alloy phase produced at 230 °C in the absence of TOP has a broad feature in the vicinity expected for elemental Rh or Co, suggesting reduction, but there are also a series of sharp peaks that match the pattern for hexamine cobalt (II) chloride, suggesting that not all of the Co gets reduced before TOP is added.

In the context of differing reactivity between the noble and base metal, the temperature of phosphidation required to produce the $Co_{2-x}Rh_xP$-phase without producing the over-phosphided CoP-phase as a byproduct was found to depend on composition. As an illustration, a representative target composition of $Co_{1.75}Rh_{0.25}P$ and three different phosphidation temperatures were chosen, while maintaining the phosphidation duration at 3 hours. Once TOP was added, a temperature of 310^{o}C was able to yield the target composition without the inclusion of any detectable impurities while higher temperatures led to a mixture of the Co_2P- and CoP-type phases. Specifically, while a temperature of 335^{o}C mostly resulted in the Co_2P-type, there was a low intensity CoP-type (211) peak evident at ~ 48^o (2Θ). On the other hand, choosing 360^{o}C as the phosphidation temperature was found to result in CoP-type as the major phase, with only a low intensity Co_2P-type (121) peak at ~42^o (2Θ) visible. Similar trends were noted by Robinson's group, where pure Co_2P nanoparticles were found to transform to CoP with increasing reaction temperature or time. [21] CoP-type byproduct formation in the other cobalt-rich compositions, i.e. where $x \leq 0.75$, was also found to depend on the phosphidation temperature, although the Co_2P phase seemed to be stabilized by increasing the Rh amount. For instance, we were able to synthesize phase pure $Co_{1.5}Rh_{0.5}P$ and $Co_{1.25}Rh_{0.75}P$ nanoparticles at 330^{o}C over 3 hours without detecting any CoP-type impurities in the samples, whereas a target composition of $Co_{1.9}Rh_{0.1}P$ had to be synthesized at 305^{o}C and for a shorter period of time, in order to yield a phase-pure product by X-rays (Fig. S2, ESI†). In contrast, over phosphidation was not apparent in the Rh-rich samples i.e. when $x \geq 1$. Specific temperature and time parameters used to achieve single-phase products for varying x are shown in Table S1 (ESI)†.

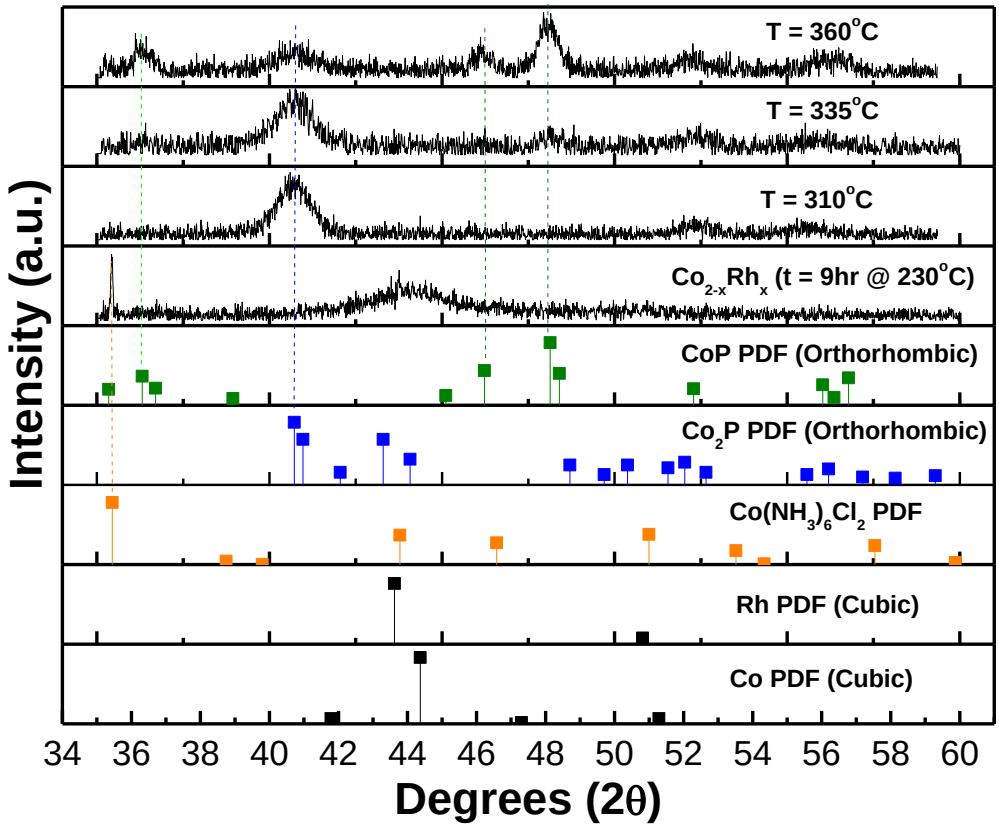

Fig. 7: PXRD data showing the effect of phosphidation temperature on the structural phase of $Co_{1.75}Rh_{0.25}P$ nanoparticles. Representative patterns for Co, Rh, $Co(NH_3)_6Cl_2$, Co_2P and CoP from the ICDD database are provided for comparison, and droplines are incorporated to guide the eye.

Catalytic activity evaluation:

We evaluated the activity of $Co_{2-x}Rh_xP$ nanoparticles towards the Oxygen Evolution Reaction (OER) in a three electrode set-up, where electrochemical measurements were performed using a rotating disk electrode. In line with our research goals, our measurements were targeted at cobalt rich $Co_{2-x}Rh_xP$ samples, since cobalt is less expensive and more earth-abundant as compared to rhodium. Shown in Fig. 8 (a) and (b) are polarization curves that were collected from selected samples, alongside the corresponding overpotential values. These values correspond to the overpotential that was needed in order to achieve a current density of 10 mA/cm^2 in each measurement and are universally accepted as figures of merit in water oxidation measurements.[33-38] These data indicate that cobalt-rich $Co_{2-x}Rh_xP$ nanoparticles offer the best activities as compared to binary end-products and Rh-rich compositions, with a sweet spot occurring at a target composition of $Co_{1.75}Rh_{0.25}P$. In addition, comparing the performance of the two binary phosphides clearly shows that Co_2P nanoparticles outperform those of Rh_2P by a relatively large margin (i.e. overpotential difference = 0.25 V). Although there are numerous reports on the OER activity of Co_2P nanoparticles in basic media,[35, 39] the same is not true for Rh_2P. As far as we could establish, the only study that has so far discussed the activity of Rh_2P nanoparticles towards the oxygen evolution reaction was carried out in acidic media (0.5 M H_2SO_4), where it was shown that Rh_2P nanoparticles were better suited for the hydrogen

evolution reaction (HER) than for OER.[29] This is not surprising given noble metal characteristics, but what is surprising is that Rh boosts the activity of Co_2P, and at relatively modest loadings.

As shown in Fig. 8 (c), Tafel slopes derived from the polarization curves are consistent with the observed general trend in the catalytic activity of the samples, with the least active one (Rh_2P) corresponding to the highest value (165 mV/dec) while the most active one ($Co_{1.75}Rh_{0.25}P$) corresponds to the lowest value (31 mV/dec). With respect to reaction microkinetics, lower Tafel slope values correspond to faster reaction rates at the electrode surface.[40-44] This is because Tafel plots represent the measured current density increase as a function of the applied potential. The slopes for the ternary phase compositions in which $x \leq 0.35$ can either be characterized as being close to 60 or 30 mV/dec, suggesting no electron transfer in the rate-determining step (rds) but a one and two electron transfer process, respectively, just prior to the rds.[35, 40] On the other hand, samples whose slopes are close to 120mV/dec ($Co_{1.5}Rh_{0.5}P$ and Co_2P) may be associated with a reaction mechanism in which the rate determining step involves a single electron transfer, with no electron transfers occurring prior.[40] Lastly, the slope for the least active sample (Rh_2P) does not correspond to any classical Tafel slope value, suggesting a complex mechanism (or competing mechanisms) and a sluggish process.

In order to ascertain that the anodic current of our most active sample ($Co_{1.75}Rh_{0.25}P$) is associated with water oxidation, bulk electrolysis was performed for 65 minutes using a two compartment H-type cell at a current density of 10 mA/cm^2 and the Faradaic efficiency was computed based on consumed charge (theoretical) and evolved oxygen gas (experimental) as shown in Fig. 8 (d). Our analysis yielded an efficiency of 97%, suggesting a high selectivity to oxygen with minimal Faradaic losses.[35, 45]

The long term stability of the above discussed sample ($Co_{1.75}Rh_{0.25}P$) was also evaluated by performing a controlled potential electrolysis experiment for 50 hours as shown in Fig. 9. Cumulatively, there was no net current density drop witnessed during the 50 hour test duration, implying that the sample was not deactivating with time during the test duration. What was surprising however was the fact that the sample was found to slowly activate with time, as can be seen from the slight increase in the current density over time as highlighted by the dashed line (overall current density increase ~10% over the 50 hour duration). As described below, this increase is attributed to changes in the catalyst during cycling.

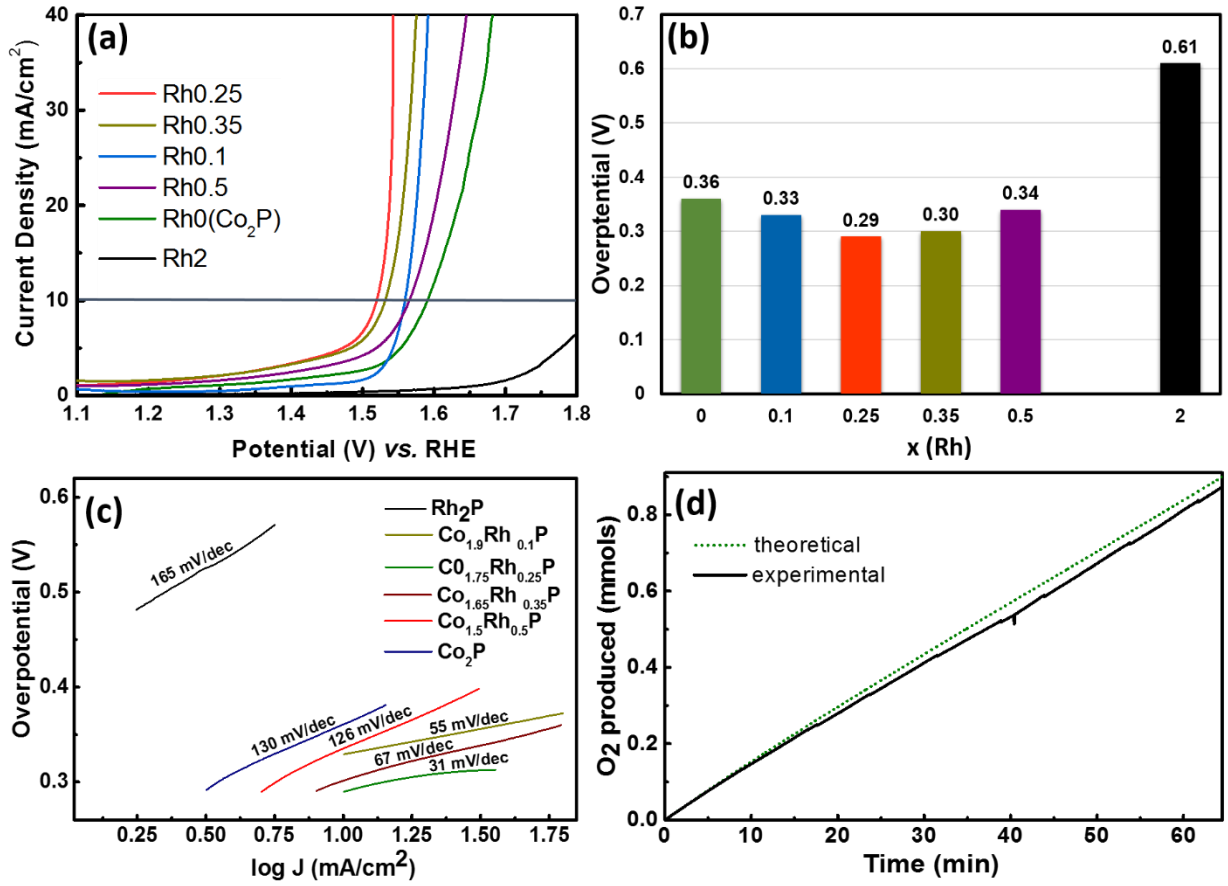

Fig. 8: (a) Water oxidation polarization curves, (b) overpotential values (at 10 mA/cm^2) for selected $Co_{2-x}Rh_xP$ nanoparticles, (c) Tafel plots derived from 8(a) and (d) Faradaic efficiency test data for $Co_{1.75}Rh_{0.25}P$.

Probing the evolving nature of the catalyst:

In order to understand the effect of the catalytic reaction on the evolution of the catalyst, X-ray Photoelectron Spectroscopy (XPS) studies were performed on the $Co_{1.75}Rh_{0.25}P$ nanoparticles, both before and after OER catalysis measurement, as summarized in Fig. 10. As far as the fresh catalyst is concerned, the Co peak that occurs at 778.8 eV ($2p_{3/2}$) corresponds to the binding energy of Co in the ternary phosphide structure while the peaks that appear at 782.5 and 787.1 eV correspond to Co^{2+} species resulting from surface oxidation.[35] The Rh peaks that occur at 307.8 eV ($3d_{3/2}$) and 312.5 eV ($3d_{1/2}$) correspond to the binding energy of Rh in the phosphide structure. The P peaks that occur at 129.9 eV ($2p_{3/2}$) and 130.7 eV ($2p_{1/2}$) correspond to phosphide species,[29, 35] whereas the P peak that occurs at 134.5 eV corresponds to phosphate or phosphite species, and is attributed to surface oxidation. Data for the spent catalyst, on the other hand, is dominated by surface oxidized species such as Co^{2+}, Rh^{3+} and P^{5+}, with the peaks for reduced Co, Rh or P species being either barely noticeable or completely diminished. These observations suggest surface chemical modifications have occurred during the OER process.

Previous reports have shown that transition metal phosphide electrocatalysts will change or deactivate over time during the OER process through the leaching of phosphate ions into the electrolyte solution. We sought to establish whether our samples go through a similar fate by

performing ICP-MS studies on a representative sample ($Co_{1.75}Rh_{0.25}P$), before and after OER electrocatalysis. Table S4 (ESI)† shows that the molar ratios for the metal ions before and after catalysis remain unchanged, suggesting they remain in the solid-state. However, the amount of P in the post-catalysis sample is completely depleted. It is clear from these data that the composition of the material changes with time, in line with what has been purported previously.[18, 35]

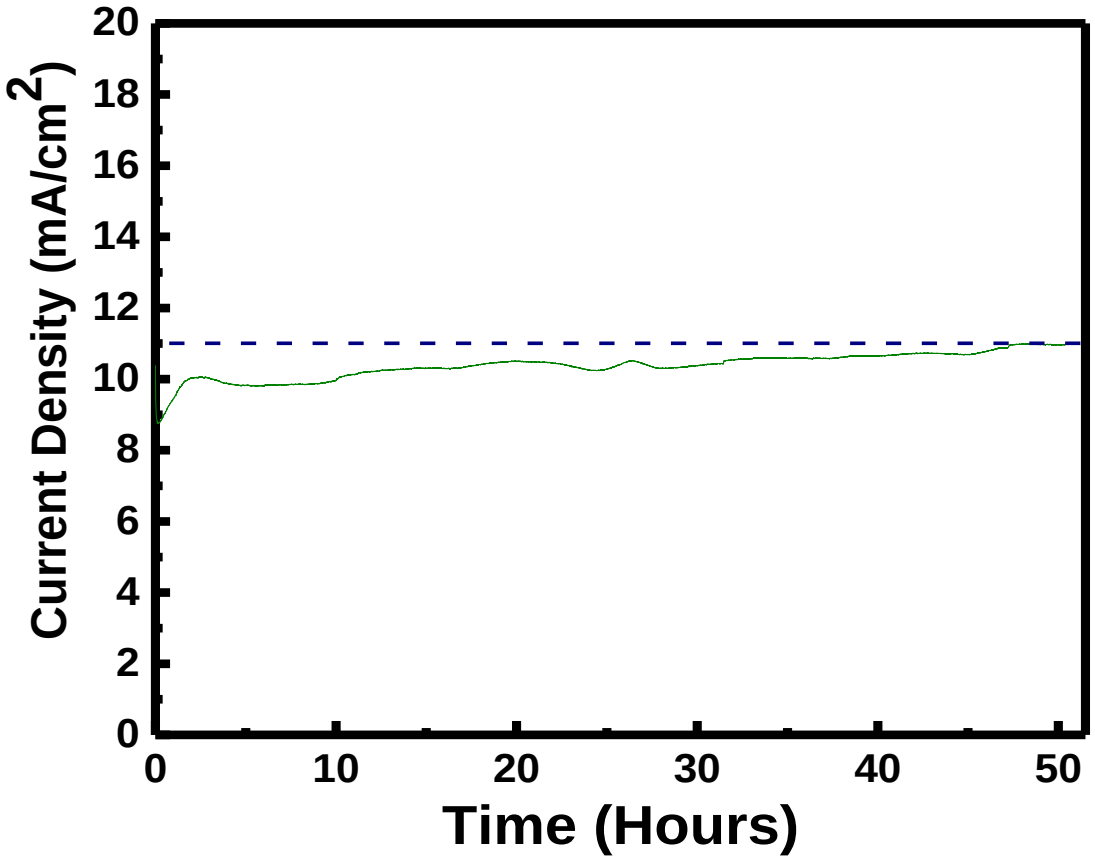

Figure 9: Long term stability test data for the $Co_{1.75}Rh_{0.25}P$ electrocatalyst at constant potential

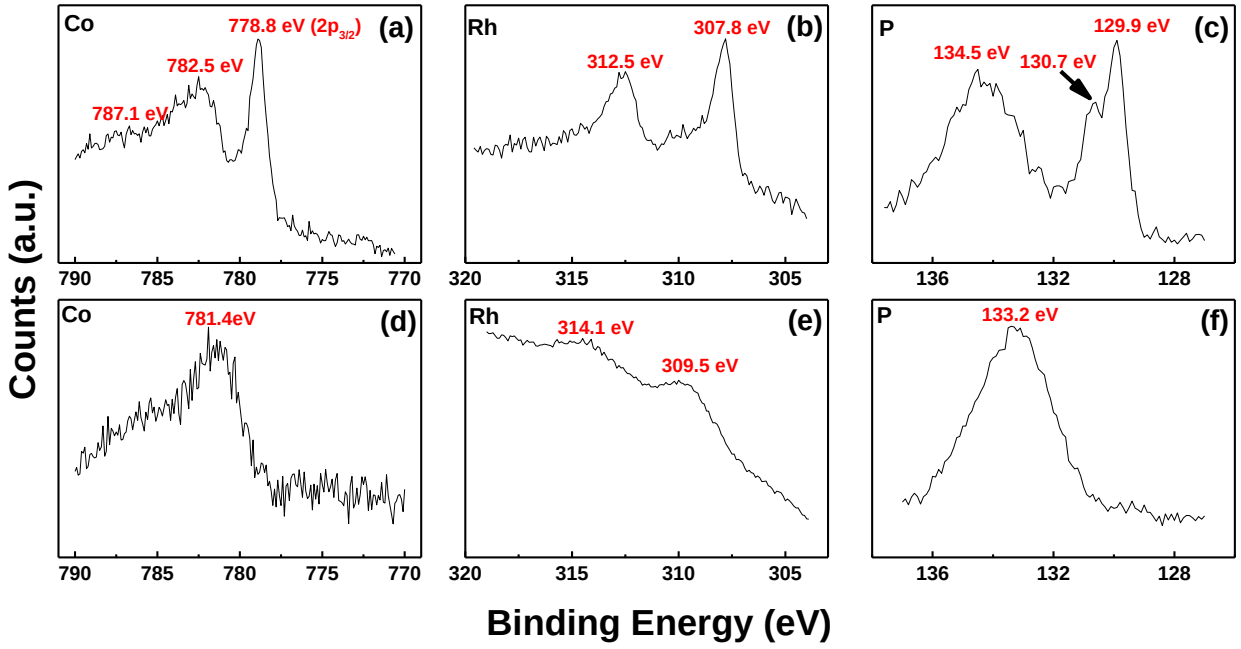

Fig. 10: XPS Data for $Co_{1.75}Rh_{0.25}P$ nanoparticles before catalysis (a-c) and after catalysis (d-f)

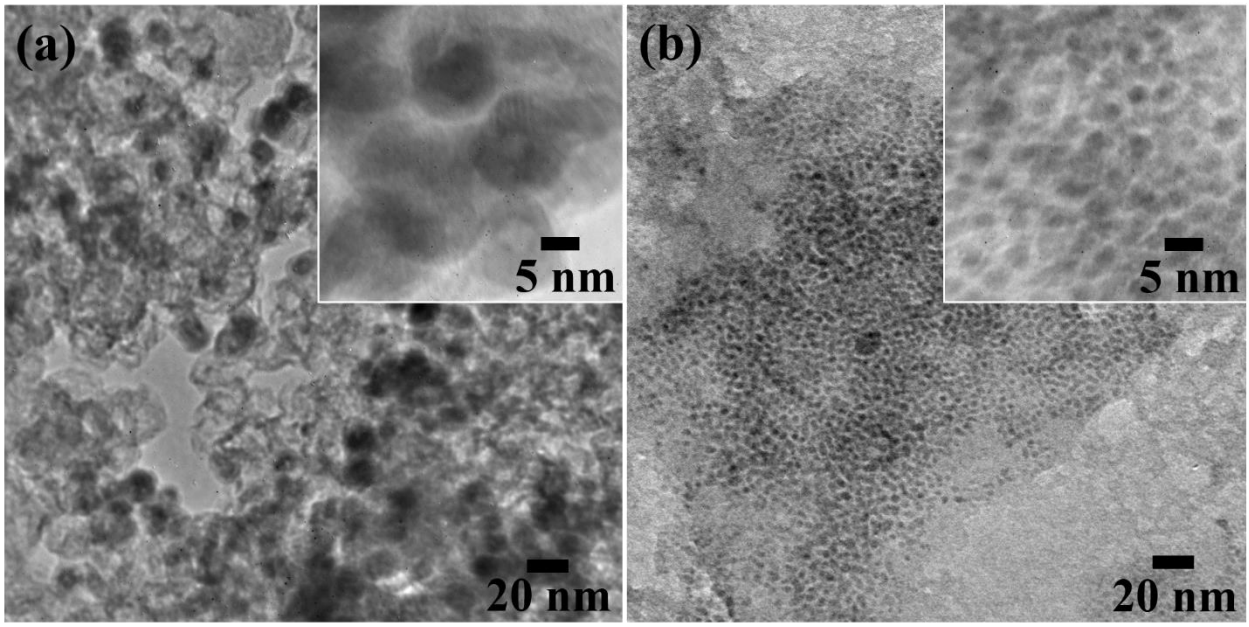

Fig. 11: TEM data for the $Co_{1.75}Rh_{0.25}P$-carbon nanocomposite (a) *before* and (b) *after* catalysis

Finally, in order to establish the morphological fate of our carbon-supported electrocatalyst nanoparticles after OER, TEM data were collected pre- and post (1 h cycling) catalysis using the $Co_{1.75}Rh_{0.25}P$-carbon nanocomposite as a representative composition. As shown in Fig. 11, the size and morphology of the nanoparticles changed significantly after OER cycling, with a reconstruction from ~10 nm hollow spheres to 2-3 nm dense spheres. Notably, there is no aggregation or sintering evident. These data, combined with the stability test data showing a modest increase in activity with time, the ICP data showing loss of phosphorus with cycling, and

the XPS data revealing oxidation, suggest that the metal phosphides serve as pre-catalysts that undergo morphological, compositional and structural changes under the highly oxidizing OER conditions, as noted for related materials,[46, 47] producing a bimetallic oxidized catalyst *in situ*. These data add to the growing body of evidence that a complex mixture of species are responsible for the unique behavior of transition metal phosphide OER catalysts.[29, 33-35]

Conclusion

It has been demonstrated that a wide range of $Co_{2-x}Rh_xP$ solid solutions can be synthesized at the nanoscale and under mild reaction conditions via the arrested precipitation technique. We have specifically demonstrated that a cubic antifluorite (Rh_2P) and an orthorhombic system (Co_2P) can be solubilized to yield $Co_{2-x}Rh_xP$ ternary phase nanoparticles of different compositions with the Co-rich phases crystallizing in the orthorhombic Fe_2P-type structure and the Rh-rich phases adopting cubic antifluorite with a structural transition near the CoRhP composition. The distinct reactivity profiles of the noble and base metal require initial pre-reduction of metal precursors by oleylamine at intermediate temperatures (230 °C) before the P-precursor (TOP) is introduced. The ternary phases are more reactive toward water oxidation than binary endproducts, with the minimum overpotential obtained for x = 0.25 (0.29V at 10mA/cm^2). Despite the fact that Rh_2P is the least active, small amounts of Rh incorporated into Co_2P nanoparticles boosted the activity, implying that the activity of the Co-rich ternary phase nanoparticles intrinsically benefits from the ternary phase structure of the nanoparticles. Detailed studies on the most active phase suggest that metal phosphides (ca 10 nm hollow structures) yield small (2-3 nm) dense metal oxides upon cycling, with increasing activity associated with either an increased number of active sites or enhanced site activity. Future studies in our group will focus on understanding the origin of the catalytic synergism that exists in cobalt-rich $Co_{2-x}Rh_xP$ nanoparticles and probing methods to augment the stability and efficiency.

Acknowledgements

This work was supported by the National Science Foundation (Grant No. CHE-1361741) and by Wayne State University, through a Rumble Fellowship. Data were collected both from the Lumigen Instrument Center at Wayne State University and from the Michigan Center for Materials Characterization at the University of Michigan. This work made use of the JEOL 2010 TEM supported by NSF Award #0216084 and the PXRD Facility supported by NSF Award #1427926.

References

1. E. Jones, *Phys. Rev.*, 1967, **158**, 295.
2. R. Gambino, T. McGuire and Y. Nakamura, *J. Appl. Phys.*, 1967, **38**, 1253-1255.
3. R. Fruchart, A. Roger and J. Senateur, *J. Appl. Phys.*, 1969, **40**, 1250-1257.
4. H. G. Von Schnering and W. Hönle, *Chem. Rev.*, 1988, **88**, 243-273.
5. S. Carenco, D. Portehault, C. Boissiere, N. Mezailles and C. Sanchez, *Chem. Rev.*, 2013, **113**, 7981-8065.
6. Y. Shi and B. Zhang, *Chem. Soc. Rev.*, 2016, **45**, 1529-1541.
7. P. Ivan, *J, Mater. Chem.*, 1994, **4**, 279-283.

8. C. Stinner, R. Prins and T. Weber, *J. Catal.*, 2001, **202**, 187-194.
9. S. T. Oyama, *J. Catal.*, 2003, **216**, 343-352.
10. A. W. Burns, A. F. Gaudette and M. E. Bussell, *J. Catal.*, 2008, **260**, 262-269.
11. A. Hitihami-Mudiyanselage, M. P. Arachchige, T. Seda, G. Lawes and S. L. Brock, *Chem. Mater.*, 2015, **27**, 6592-6600.
12. S. J. Danforth, D. R. Liyanage, A. Hitihami-Mudiyanselage, B. Ilic, S. L. Brock and M. E. Bussell, *Surf. Sci.*, 2016, **648**, 126-135.
13. D. R. Liyanage, S. J. Danforth, Y. Liu, M. E. Bussell and S. L. Brock, *Chem. Mater.*, 2015, **27**, 4349-4357.
14. J. R. Hayes, R. H. Bowker, A. F. Gaudette, M. C. Smith, C. E. Moak, C. Y. Nam, T. K. Pratum and M. E. Bussell, *J. Catal.*, 2010, **276**, 249-258.
15. Y. Kanda, C. Temma, K. Nakata, T. Kobayashi, M. Sugioka and Y. Uemichi, *Appl. Catal., A*, 2010, **386**, 171-178.
16. D. Wang and Y. Li, *Inorg. Chem.*, 2011, **50**, 5196-5202.
17. D. Wang, Q. Peng and Y. Li, *Nano Res.*, 2010, **3**, 574-580.
18. D. R. Liyanage, D. Li, Q. B. Cheek, H. Baydoun and S. L. Brock, *J. Mater. Chem., A.*, 2017, **5**, 17609-17618.
19. S. Ohta and H. Onmayashiki, *Physica B*, 1998, **253**, 193-202.
20. H. Nishihara, T. Yoshida, T. Matsukawa, T. Kanomata, G. Strijkers, W. De Jonge, F. Wagatsuma and T. Shinohara, *J. Alloys Compd.*, 2001, **317**, 258-261.
21. D.-H. Ha, L. M. Moreau, C. R. Bealing, H. Zhang, R. G. Hennig and R. D. Robinson, *J, Mater. Chem.*, 2011, **21**, 11498-11510.
22. A. E. Henkes, Y. Vasquez and R. E. Schaak, *J. Am. Chem. Soc.*, 2007, **129**, 1896-1897.
23. P. E. Blanchard, A. P. Grosvenor, R. G. Cavell and A. Mar, *J, Mater. Chem.*, 2009, **19**, 6015-6022.
24. Y. Xia, T. D. Nguyen, M. Yang, B. Lee, A. Santos, P. Podsiadlo, Z. Tang, S. C. Glotzer and N. A. Kotov, *Nat. Nanotechnol.*, 2011, **6**, 580.
25. T. Wang, D. LaMontagne, J. Lynch, J. Zhuang and Y. C. Cao, *Chem. Soc. Rev.*, 2013, **42**, 2804-2823.
26. W. Yang, Y. Huang, J. Fan, Y. Yu, C. Yang and H. Li, *Nanoscale*, 2016, **8**, 4898-4902.
27. D. Das, A. Das, M. Reghunath and K. K. Nanda, *Green Chem,*, 2017, **19**, 1327-1335.
28. S. E. Habas, F. G. Baddour, D. A. Ruddy, C. P. Nash, J. Wang, M. Pan, J. E. Hensley and J. A. Schaidle, *Chem. Mater.*, 2015, **27**, 7580-7592.
29. H. Duan, D. Li, Y. Tang, Y. He, S. Ji, R. Wang, H. Lv, P. P. Lopes, A. P. Paulikas and H. Li, *J. Am. Chem. Soc.*, 2017, **139**, 5494-5502.
30. H. Zhang, D.-H. Ha, R. Hovden, L. F. Kourkoutis and R. D. Robinson, *Nano Lett.*, 2010, **11**, 188-197.
31. S. C. Perera, G. Tsoi, L. E. Wenger and S. L. Brock, *J. Am. Chem. Soc.*, 2003, **125**, 13960-13961.
32. S. C. Perera, P. S. Fodor, G. M. Tsoi, L. E. Wenger and S. L. Brock, *Chem. Mater.*, 2003, **15**, 4034-4038.
33. J. Kibsgaard, C. Tsai, K. Chan, J. D. Benck, J. K. Nørskov, F. Abild-Pedersen and T. F. Jaramillo, *Energy Environ. Sci.*, 2015, **8**, 3022-3029.
34. A. Mendoza-Garcia, D. Su and S. Sun, *Nanoscale*, 2016, **8**, 3244-3247.
35. D. Li, H. Baydoun, C. u. N. Verani and S. L. Brock, *J. Am. Chem. Soc.*, 2016, **138**, 4006-4009.

36. T. Liu, L. Xie, J. Yang, R. Kong, G. Du, A. M. Asiri, X. Sun and L. Chen, *ChemElectroChem*, 2017, **4**, 1840-1845.
37. G. Zhang, G. Wang, Y. Liu, H. Liu, J. Qu and J. Li, *J. Am. Chem. Soc.*, 2016, **138**, 14686-14693.
38. P. Cai, J. Huang, J. Chen and Z. Wen, *Angew. Chem. Int. Ed.*, 2017, **56**, 4858-4861.
39. X. Li, Y. Fang, F. Li, M. Tian, X. Long, J. Jin and J. Ma, *J. Mater. Chem., A.*, 2016, **4**, 15501-15510.
40. Y.-H. Fang and Z.-P. Liu, *ACS Catal.*, 2014, **4**, 4364-4376.
41. T. Shinagawa, A. T. Garcia-Esparza and K. Takanabe, *Sci. Rep.*, 2015, **5**, 13801.
42. L. Ye and Z. Wen, *Electrochem Commun*, 2017, **83**, 85-89.
43. C. Tang, R. Zhang, W. Lu, L. He, X. Jiang, A. M. Asiri and X. Sun, *Adv. Mater.*, 2017, **29**.
44. X. Xiong, Y. Ji, M. Xie, C. You, L. Yang, Z. Liu, A. M. Asiri and X. Sun, *Electrochem Commun*, 2018, **86**, 161-165.
45. F. Song and X. Hu, *Nat. Commun.*, 2014, **5**, 4477.
46. H. Wang, H.-W. Lee, Y. Deng, Z. Lu, P.-C. Hsu, Y. Liu, D. Lin and Y. Cui, *Nat. Commun.*, 2015, **6**, 7261.
47. H. Schäfer, K. Küpper, K. Müller-Buschbaum, D. Daum, M. Steinhart, J. Wollschläger, U. Krupp, M. Schmidt, W. Han and J. Stangl, *Nanoscale*, 2017, **9**, 17829-17838.

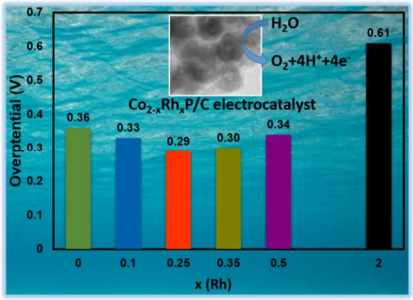

Incorporation of small amounts of Rh results in a significant improvement in the electrocatalytic activity of Co_2P for water oxidation.